Materials Research Bulletin 106 (2018) 40–48

Contents lists available at ScienceDirect

Materials Research Bulletin

journal homepage: www.elsevier.com/locate/matresbu

Hydrogen titanate nanotubes for dye sensitized solar cells applications: Experimental and theoretical study

Fernando Pignanelli[a], Luciana Fernández-Werner[a,*], Mariano Romero[a], Dominique Mombrú[a], Milton A. Tumelero[b,c], André A. Pasa[c], Estefanía Germán[a,d], Ricardo Faccio[a,*], Álvaro W. Mombrú[a,*]

[a] Centro NanoMat, DETEMA, Facultad de Química, Universidad de la República, Montevideo, Uruguay
[b] Instituto de Física – Universidade Federal do Rio Grande do Sul (UFRGS), Porto Alegre C.P. 91501-970, Brazil
[c] Laboratório de Filmes Finos e Superficies – Departamento de Física–Universidade Federal de Santa Catarina (UFSC), Florianópolis C.P. 88040-900, Brazil
[d] Departamento de Física, Universidad Nacional del Sur & IFISUR (UNS-CONICET), Av. Alem 1253, 8000, Bahía Blanca, Argentina

ARTICLE INFO

Keywords:
Hydrogen titanate nanotubes
Solar cells
DFT calculations

ABSTRACT

The existent research literature of Dye Sensitized Solar Cells (DSSC) is mainly focused on the dye but there are very few studies focused in the semiconductor. Here, we present the performance of hydrogen titanate nanotubes (HTNT), showing an enhancement of the solar cell efficiency from 5.95% to 7.63%, respect to anatase as photoelectrode. This enhancement could be explained in terms of open-circuit voltage, directly associated to the value of the HTNT band gap (E_g = 3.3 eV), the relative position of the edge conduction band; and the increase of the short-circuit current, directly associated to the enhancement of the specific area of the photoelectrode. All these characteristics are in very good concordance with our theoretical modelling of the system, based on First Principles calculations. We expect that this system could be further characterized, utilizing different dyes or absorbers, in order to evaluate the potential use of hydrogen titanate nanotubes for solar cell applications.

1. Introduction

Since first introduced by Grätzel and O'Reagan in earliest 90' [1], dye-sensitized solar cells (DSSCs) have been intensively studied due to their interesting optical properties and that they are comparatively cheaper than silicon photovoltaic solar cells. Additionally, it has a high photon to electrical energy conversion, reaching a maximum overall efficiency of- 13% [2]. The DSSC essentially consists of a semiconductor based photoanode covered with a monolayer of dye, an electrolyte and counter electrode. Photoexcitation of the dye promotes the injection of an electron from the LUMO of the dye to the conduction band of the semiconductor. The dye is regenerated by the donation of an electron from the redox electrolyte and the reduction of the electrolyte by the counter electrode completes the process. Electrolyte that contains triiodide/iodide as a redox pair is commonly used. The open circuit voltage is determined by the difference between the Fermi level of the semiconductor and the redox potential of the electrolyte. Due to the large interest and the volume of work regarding the optimization of each component and assembly procedures, several reviews are focused on recent improvements and developments of DSSC [3–5]. One example, is the novel use of hybrid organic/inorganic compounds involving metal oxide mixed with organic polymer nanocomposites [6].

Among the semiconductors chosen for photoanode construction, TiO_2 has been widely preferred. It presents a wide bandgap, in which the conduction band (CB) edge, is principally contributed from O-2p orbitals, while the valence band (VB) edge is majorly contributed from Ti-3d orbitals. The difference in parity between states in the CB and VB lead to differences in the symmetry of electron and hole states, resulting in a reduction of the recombination probability [7]. Among the options of TiO_2 polymorphs and particle morphologies, one-dimensional nanostructure have attracted the attention due the attempt to improve electron diffusion coefficients due to directional electron mobility as well as shrinking inter-crystallite contacts, lowering the recombination probability and accelerating electron transport [8].

In reference to one-dimensional structures, major efforts have been done to grow self-organized TiO_2 nanotube layers by anodic oxidation of a Ti-metal sheet finding overall solar cells efficiencies of 2–3% under AM 1.5 illumination [9–15]. When the tubes are decorated with TiO_2 nanoparticles using a $TiCl_4$ treatment [16–20], [21], in order to increase surface area, efficiencies up to 5% have been reached [8]. Efficiency of 9.1% was reported by Lin et al [22] using transparent electrode of open-ended TiNT (Titania Nanotubes) film that was strongly

* Corresponding authors.
E-mail addresses: lucianaf@fq.edu.uy (L. Fernández-Werner), rfaccio@fq.edu.uy (R. Faccio), amombru@fq.edu.uy (Á.W. Mombrú).

https://doi.org/10.1016/j.materresbull.2018.05.029
Received 11 March 2018; Received in revised form 16 May 2018; Accepted 25 May 2018
Available online 26 May 2018

interconnected onto FTO (Fluorine doped Tin Oxide) glass by a TiO_2 nanoparticle (NP-TiO_2) under layer. Multidirectional orientation of TiO_2 nanotubes obtained by chemical methods such as hydrothermal methods reached comparably high efficiency solar cells, despite the fact that they do not necessarily lead to unidirectional electron flow to the back contact. However, using these methods it is possible to obtain nanotubes with smaller diameters increasing the surface area and consequently the dye loading.

In this work, we employ hydrogen trititanate nanotubes (HTNT) obtained by hydrothermal methods as materials for anode of DSSC reaching comparatively larger overall cell efficiency than using anatase nanoparticles.

The manuscript is organized as follows. Section 2 describes de methodology for the preparation of HTNT (2.1) and then the preparation of the corresponding photoanode (2.2), next we describe the structural and physical characterization (2.3).In the case of the structural characterization we discuss: X-ray diffraction (2.3.1), Raman Microscopy (2.3.2), AFM/TEM/SEM (2.3.3). The idea is to demonstrate that the HTNT keeps their structure and functionality after the photoanode treatment. The physical and optical characterization is presented in Section (2.4). Results and discussion are presented in the Section 3, with an analogous structure of the precedent Section 2. Finally, Section 4 presents the main conclusions.

2. Methods

2.1. Synthesis of HTNT

Titanate nanotubes were synthesized via hydrothermal method, following the procedure previously informed by some authors of this work [23] using commercial TiO_2 anatase nano powder from Sigma-Aldrich® [Titanium(IV) oxide, anatase (External ID: 232033_ALDRICH)] as the precursor material. Briefly, 1.25 *g* r of TiO_2 nanopowder was dispersed using ultrasonication on 75 mL of NaOH 10 M in a Teflon lined autoclave using a 2/3 fill factor for the reactor. The reactor was kept at 145 °C for 24 h s with slight constant stirring of 120rev.min^{-1} and then, air cooled to ambient temperature. The solid was separated through centrifugation, fractioned and then thoroughly washed with HCl 0.1 M and distilled water reaching a final pH ~ 4. Finally, the sample was dried at 50 °C, for more details please see L. Fernández-Werner et al [23].

2.2. Prototype preparation

Photoelectrodes were composed of two layers of semiconductors on top of a FTO conductive glass. The first layer, for both cells, consist of a compact layer of anatase nanoparticles deposited by spin coating using the commercially available "Titanium(IV) oxide nanopowder" (External ID: 718467_ALDRICH) suspended in distilled water. These films were sintered at 400 °C during 2 h. The second layer, for both cases,was applied using "Doctor Blade" method [24] with small quantities of ethylene glycol as surfactant, utilizing 62.5 μm "3 M Scotch Magic Tape" as separator. For the case of anatase photoelectrode, Sigma-Aldrich® Titanium(IV) oxide, anatase (External ID: 232033_ALDRICH) was used for the second layer and it was sintered at 400 °C during 3 h. In the case of HTNT photoelectrode, the obtained HTNT was used for this second layer and the film was sintered at 110 °C during 3 h. After that, in both cases, the photoelectrodes were dipped into a solution containing 10 mg of "DyeSol N719″ dye in 25 ml of absolute ethanol for 12 h s in darkness.

Counter electrodes consist of a thin film of gold made by Sputtering deposition on FTO conductive glass. At the interface between both electrodes, we use a solution of I^-/I_3- in absolute ethanol ("DyeSol EL-141″) as electrolyte and the obtained sandwiched solar cells showed an active area of 3.25cm^2.

2.3. Structural and physical characterization

2.3.1. X-ray powder diffraction (XRPD)

X-ray Powder diffraction (XRPD) measurements were taken using a Rigaku Ultima IV diffraction system operating with CuKα radiation. The XRPD scans were performed in the range 2θ = 5.00–80.00°, angle step of 0.02° and time step of 40 s per step.

2.3.2. Confocal Raman microscopy

Confocal Raman Microscopy was performed using WITec Alpha 300-RA confocal Raman Imaging system. The excitation laser wavelength corresponds to λ = 532 nm and the power was adjusted to 45 mW to avoid sample decomposition and dehydration. Raman spectra were obtained by calculating the average of a set of 22,500 spectra with 0.053 s integration time for each spectrum. The spectrometer operating with a grating of 600 lines per mm allowed us to obtain a resolution of ~4 cm^{-1} in the range of 70 cm^{-1} to 4000 cm^{-1}. All the confocal Raman images were collected at the resolution optical limit down to 300 nm.

2.3.3. Atomic force microscopy (AFM), transmission electron miscroscopy (TEM) and scanning electron microscopy (SEM)

AFM images were obtained using Confocal Raman Microscopy with Atomic Force Microscopy equipment WITec Alpha 300 RA, operating in a non-contact AC mode. All the presented figures correspond to 2 μm x 2 μm utilizing a grid of 150 × 150 grid points.

TEM images were obtained using a JEOL JEM 1010 with 100 kV of acceleration voltage and high resolution images were obtained using a JEOL JEM-2010 with 200 kV of acceleration voltage. For the acquisition of images, the sample was dispersed in ethanol and dropping onto a carbon film supported by a copper grid. SEM images were collected in a JEOL JCM 6000 plus, taken from the as prepared photoanodes.

2.3.4. Photovoltaic characterization

UV-VIS spectra were measured by a Lambda-750 (Perkin-Elmer). Current-voltage curves (I–V) of solar cells were obtained using a source meter (Keithley 2400). A *SOLAR LIGHT LS1000-4S-005* solar simulator, with a Xe lamp and an AM1.5 filter, was used as the light source.

Electrochemical Impedance Spectroscopy (EIS) studies were obtained utilizing a Reference 3000 Gamry equipment operating in the range of 1 mHz to 10 kHz, with an AC amplitude of 10 mV, working in dark and 0.1 W·cm^{-2} illumination conditions.

2.4. Computational simulations

We simulated the electronic structure of anatase and HTNT electrodes by performing *ab initio* calculations within the Density Functional Theory (DFT) [25,26]. The calculations were made utilizing the VASP code (Vienna *ab initio* Simulation Package) [27–31]. The projector augmented wave (PAW) method[32,33] was employed to account for the electron–ion core interaction, utilizing the GGA (Generalized Gradient Approximations) exchange-correlation functional with the PBE parameterization (Perdew-Burke-Ernzerhof) [34,35]. We used the PAW-PBE potentials with the following valence electrons: Ti ($3s^2 3p^6 4s^2 3d^2$), O ($2s^2 2p^4$) and H ($1s^1$). In order to treat the strong on-site Coulomb interaction of localized electrons in transition metal oxides, which is not properly described by the GGA (and LDA) approach and affects the electronic structure, the GGA + U method proposed by Dudarev et al.[36] was used. Setting a U-parameter of 4 eV for 3*d* level of Ti for anatase and a U-parameter of 5 eV in hydrogen titanate, the multiple occupation of *d*-orbitals is penalized, and thus, the band gap width takes values closer than the experimental ones, attenuating the underestimation of this width, as well as the electron delocalization according to early works from our group[37,38]. The k-space grid of 4 × 4x1 was selected in all the calculations and also a cut-off energy for the plane wave expansion of 400 eV. The structures were optimized

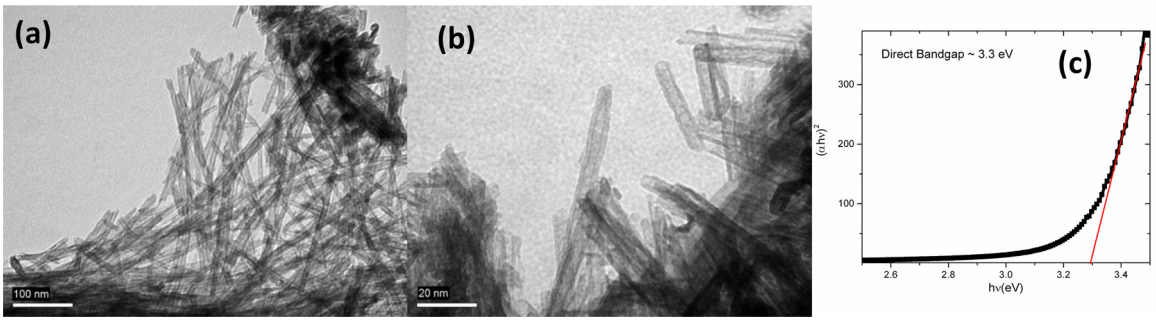

Fig. 1. - TEM images for HTNT at two different magnification (a) and (b), showing the tubular structure and the main distances. (c) The Tauc plot for the HTNT confirming direct band gap of E_g = 3.3 eV.

until the forces in all the atoms were lower than 0.01 eV.Å^{-1}, and the unit cell was optimized until the components of the stress tensor were lower than 1 kBar. In all the cases, for the simulation of the slabs, a vacuum space of 15 Å was selected in concordance with early works [37,38]. In the case of anatase (101) the periodic cell parameters correspond to a = 3.805 Å, b = 10.511 Å and c = 18.247 Å; in the case of the H-TNT the cell parameters correspond to a = 3.820 Å, b = 9.404 Å and c = 30.505 Å; in all the cases de c-axis correspond to the direction in the vacuum region.

3. Results and discussion

3.1. Structural characterization of the HTNTs

We followed the same steps for the preparation of hydrogen titanate nanotubes, according to Fernández-Werner et al [23]. We obtained, almost in one step, the nanotubes with the following chemical formula: $H_2Ti_3O_7$. $\frac{1}{2}$ H_2O (HTNT). In reference to microstructure and morphology the HTNT presents open endings with ~100 to 200 nm length, with an inner and outer diameter of 6(1) and 12(2) nm, see Fig. 1 (a) and (b),see Fig. 1 for TEM images. These results were confirmed by XRPD, TEM, and Small Angle X-ray Scattering (SAXS)and were in very good agreement with the surface area analysis determined by BET of 286 m^2 gr^{-1} [23].

Fig. 1(c) shows the Tauc plot for the HTNT, demonstrating that the nanotubes present a direct band gap of E_g = 3.3 eV. This value is in principle very good, since it is very close for the anatase nanoparticles that are usually used for the preparation of DSSC's photoelectrodes. Although it is an important parameter, it is not the only relevant one as we will discuss further in detail when discussing about the electronic structure of the HTNT.

As stated before, the aim of this work is to demonstrate the enhancement of the solar cell efficiency by changing anatase TiO_2 nanoparticles for HTNT as the second layer of the photoelectrode. The first step consists in demonstrating that the photoelectrode keeps the HTNT structure after the sintering and sensitization processes. Fig. 2(a) presents the XRPD data for the sintered photoelectrode. As stated before, this pattern could be associated to the HTNT, in concordance with a ours previously discussed methodology [23]. Applying the full pattern profile fitting we obtained the following structural parameters: d_{int} ~ 6(1)nm, d_{ext} ~ 12(1)nm and e ~ 3(1)nm, corresponding to internal diameter, external diameter and width respectively [23].Here it is important to mention, that fitting is reasonably, taking into account small differences between experimental ($I_{exp.}$) and calculated intensities ($I_{teo.}$), see Fig. 2(a).

Fig. 2(b), presents the Raman spectra for both the as prepared and the sintered photoelectrode based on HTNT. In the spectra, the presence of bands located at: 200, 283, 465, 678, 705, 846 and 935 cm^{-1}, can be seen. As demonstrated before [23], these peaks could be associated to HTNT, and they remain after the thermal treatment, confirming that the photoelectrode is based on the HTNT.

In order to confirm the homogeneity of the sample, we obtained several confocal Raman images of selected areas of 10 µm x 10 µm utilizing a grid of 80 × 80 points. Then we proceeded with a Principal Component Analysis (PCA) in order to search for minor but statistically relevant differences in the sample. As observed in Fig. 3, only one component contributes with more than 95% of the variance in the sample. This PCA component can be represented with almost all the selected area. This is a confirmation of the homogeneity of the sample. The rest of the image, marked in blue, can be attributed to the PCA component #2, and the corresponding average spectra corresponds to a Raman spectrum analogous to component #1. The difference arises from the absolute intensities, which are generated for the variations in height in the sample (focal plane) due to the porosity of the pellet prepared for the analysis. This is a demonstration of the structural homogeneity of the HTNT photoelectrode.

The AFM and SEM images for both photoelectrodes are presented in Fig. 4 for comparison. As observed, the topography of both photoelectrodes is quite different. The anatase-photoelectrode is characterized by the sintering of uniform nanoparticles; this characteristic feature is more evident from the phase contrast image, Fig. 4(b) and 4(d). When analyzing the HTNT-photoelectrode, the situation is different, since there is no evident presence of large nanoparticles as in the case of anatase. After a surface roughness analysis, the true surface is determined as 50% and 78% higher for anatase and HTNT, respectively, expressed in terms of the reference surface originally selected for the AFM measurement. These results, were further confirmed by SEM analysis on the photoelectrodes, see Fig. 4(f) and 4(g), showing a rougher surface for HTNT in comparison to anatase. This fact demonstrates how the use of the HTNT allows us to obtain a highly porous photoelectrode, in reference to the one based on anatase, that could be good for increasing the coverage surface when sensitizing with the N719 dye.

3.2. Electrical and electrochemical characterization

Fig. 5 presents the I–V curves for anatase and HTNT DSSCs, including the corresponding equivalent circuit fittings on each case and Table 1 summarize the final results, see Fig. 5(f) and (g) for the utilized circuit models. In all the cases, we include the comparison of the HTNT cell with the corresponding one utilizing anatase, to demonstrate that we are using the same conditions. In the case of anatase photoanode, the DSSC showed an efficiency of ~6%, and with the utilization of HTNT as photoelectrode the efficiency yields ~ 7.6% together with an enhancement of all the relevant photovoltaic cell efficiency parameters, as summarized in Table I. It is observed that the HTNT-DSSC shows an enhancement on maximum voltage (V_{max}), open-circuit voltage (V_{oc}), short-circuit current density (J_{sc}) and maximum current density (J_{max}), the only parameter that shows a decrease is the fill factor (FF). Based on these results, we can explain this enhancement mainly on the high specific area of the HTNT. Additionally, the increase of the V_{oc} is not obvious at first instance, since the HTNT band gap is very similar to

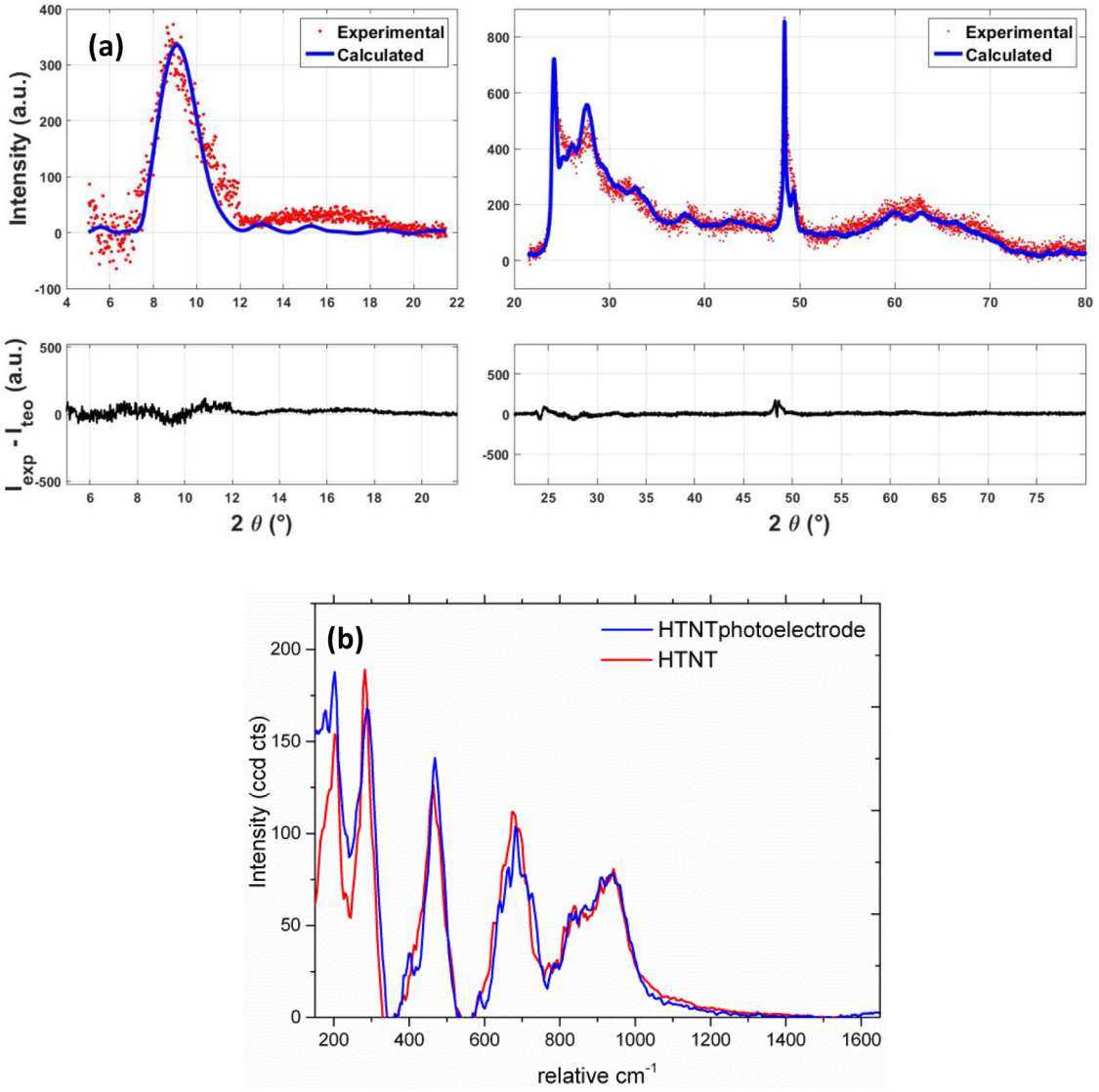

Fig. 2. -(a) XRPD pattern and fitting for the prepared photoelectrode, confirming the structure of the HTNT. The image includes the experimental data (circles) and the theoretical x-ray powder diffraction fitting (lines), including the corresponding difference curve ($I_{exp.} - I_{calc.}$). (b) Raman spectra collected for the as prepared HTNT and the sintered HTNT photoelectrode.

anatase, this is showed in Fig. 6. This issue will be addressed and discussed again in the theoretical section of this work. Table 1 also includes the effect of series and shunt resistance (R_s and R_{sh}). The series resistance should be as low as possible, and the shunt resistance(R_{sh}) it is expected to be very high, in order to reduce the alternative electronic path in the photoelectrode. According to the parameters obtained from the equivalent circuit fitting (Fig. 4(f)), the series resistance for anatase and HTNTs are very similar (Table 1), even slightly better for HTNT. On the other hand, the shunt resistance for HTNT is approximately ~47% lower than anatase, the obtained values correspond to 2.73(10) kΩ and 1.27(2) kΩ for anatase and HTNT respectively. It does not seem to be the ideal situation, in terms of the resistance, explaining the reason why the FF obtained for HTNT is lower in comparison to the one for anatase. Nevertheless, the improvement in the value of V_{oc} and J_{sc} are high enough so that the efficiency of HTNT are still greater than anatase, even though the FF is somewhat lower.

Electrochemical impedance spectroscopy (EIS) was performed in order to further characterize the electrochemical behavior of the (Anatase or HTNT)/dye/electrolyte interfaces. Electrochemical impedance versus applied DC bias for anatase- and HTNT-DSSC solar cells under illumination conditions is shown in Fig. 6(a) and (b), respectively. In addition, the main parameters obtained from the EIS fitting for anatase- and HTNT-DSSC solar cells under dark and illumination conditions are shown in Table 2. The corresponding equivalent circuit used to fit the impedance spectrum is shown in Fig. 6(e), for describing the region of counter electrode, electrolyte diffusion, charge transfer between electrolyte/dye/photoelectrode and photoanode; all of them described by electric resistance (R), constant phase element (CPE) and Warburg diffusion (W). It basically consists in the combination of three main contributions; the first ascribed to the charge transfer at the photoanode, the second is ascribed to I^-/I^{3-} diffusion process in the electrolyte and the third is ascribed to the electron transfer at the counter electrode, as typically reported for other DSSC devices [39–41].

According to Wang et al [41], different processes occur in the cell in the dark or under illumination. Under dark conditions, the electrons are basically transported through the mesoscopic electrode and react with I_3^- while, at the same time, I^- is oxidized to I_3^- at the counter electrode. Under illumination conditions, as the applied bias approaches the open circuit voltage, there is a net current reduction and more injected electrons are recaptured by I^{3-} before being extracted to the external circuit. This fact can be confirmed by inspection of the Nyquist

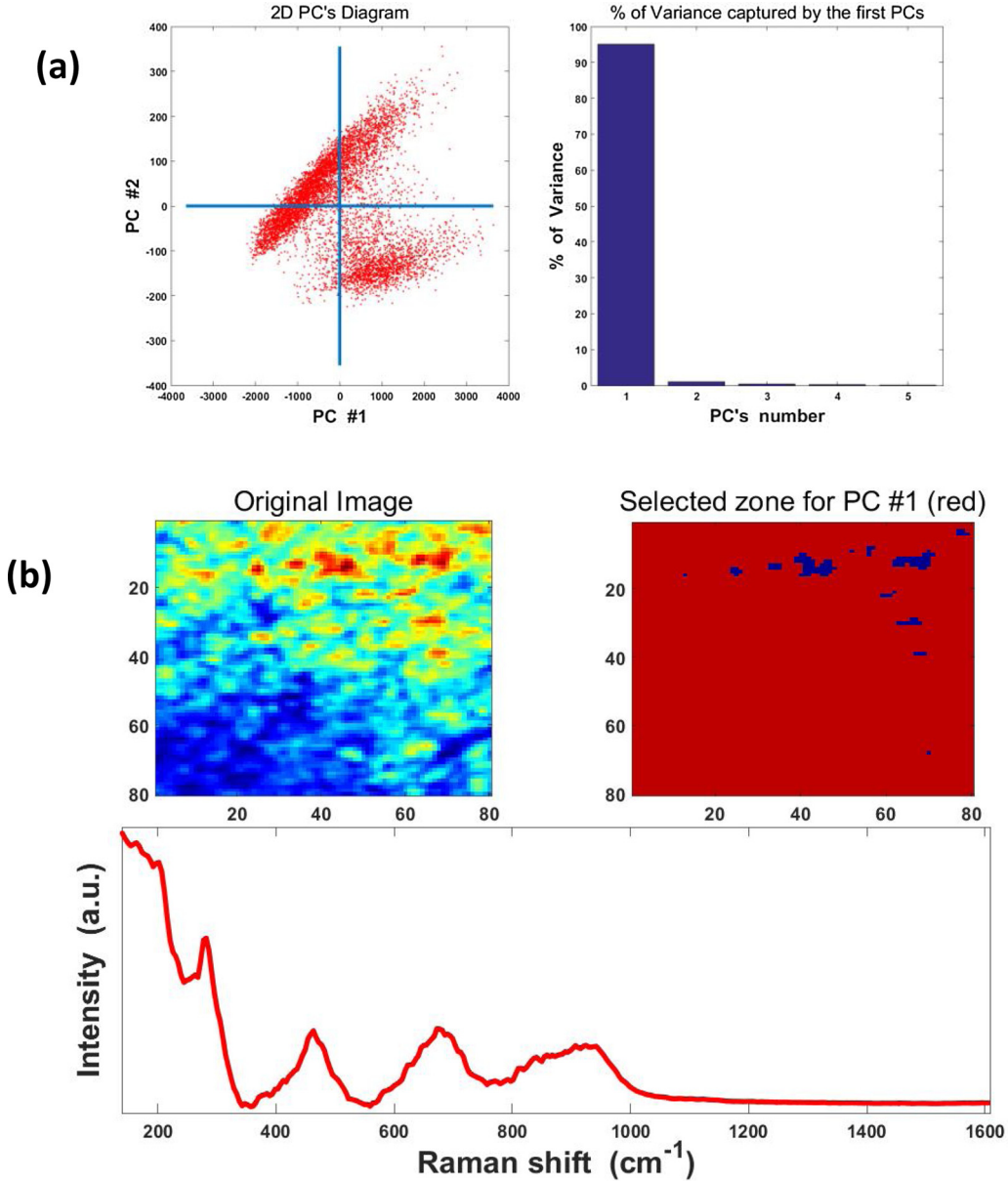

Fig. 3. (a) Two-dimensional diagram of the representing the main contributions to the PCA and the associated % of variance corresponding to each component. (b) Reconstructed image from component #1 of the PCA, the mask of the selected area and the corresponding average Raman spectra.

Plot, that shows a decrease of semicircle radius at intermediate frequencies for the applied bias condition, meanwhile the oxidized dye is regenerated by I^-. Moreover, there is a slight decrease in the resistance (R_D) associated to the charge transfer between electrolyte-dye-photoelectrode for HTNT- respect to anatase-DSSC, as shown in Table 2. Here, it is important to mention that, the direct comparison between resistances (RD) between anatase and HTNT is valid, since the same procedure for the photoanode preparation was utilized.

When comparing the bode phase plots of the anatase and HTNT prototypes, at the same applied potential of 550 mV (see Figs. 6(c) and (d)), both under illumination present a shift towards higher frequencies of the main peak. As discussed by Wang et al [41], this can be ascribed to a difference in the local I_3^- concentration. Under illumination condition, I_3^- is formed 'in situ' by dye regeneration at the mesoporous-electrode/electrolyte interface, whereas in the dark, I_3^- is generated at counter electrode and penetrates the working electrode by a diffusion process. As presented in Table 2, we can see that this effect is more noticeable for the HTNT-DSSC prototype, possibly due to a better porosity of the photoelectrode (early confirmed by AFM and SEM),that provides more active sites where the recombination could take place.

3.3. Computational simulations

As stated before, performing ab initio calculations allows to understand the difference between electrodes, in term of their electronic structure. As can be observed, all the cell parameters are in good concordance with prior results [37,38]. As described in the methodology, we applied DFT + U to the Ti-d levels in order to get and reproduce the experimental band gap, without utilizing highly demanding hybrid exchange-correlation functionals. We successfully applied this methodology to a series of TiO_2 polymorphs and H-titanates [37,38]. The Projected Density of States (PDOS) indicates a very similar band gap, same as observed in the experiment. Additionally, it was observed a similar charge state distribution, since the valence band is majorly contributed from oxygen p-states, and the conduction band is majorly contributed from the Ti-d states, see Fig. 7.

A deep analysis, involving the estimation of the work function Φ_{work}, could give us information about the origin of the differences

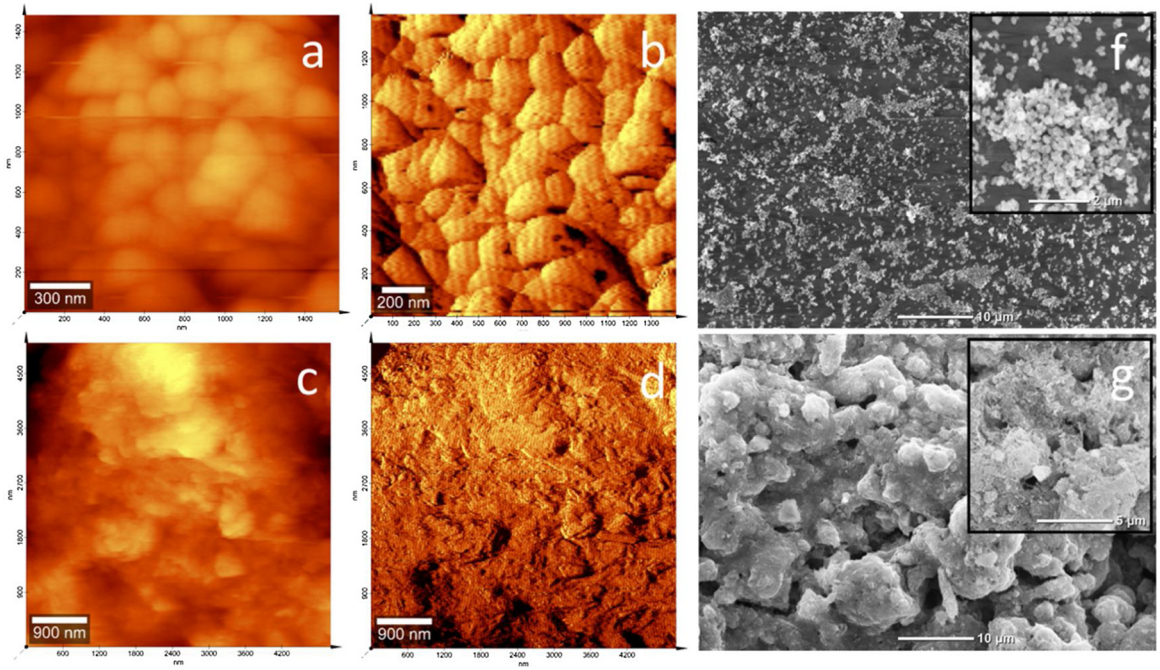

Fig. 4. - AFM images for the anatase photoelectrode: (a) topography, (b) phase contrast. Idem for HTNT photoelectrode (c) topography and (d) phase contrast. SEM images for (f) anatase and (g) HTNT are presented at two magnifications respectively.

observed in the photoelectric response of both electrodes. The Φ_{work} does not only tell us about the ionization potential of the surfaces, but it can be used to analyze the band alignment of the different components of the electrodes, since it establishes the reference of the vacuum region. As can be observed, the $\Phi_{HTNT} < \Phi_{anatase}$, the upward movement of the E_{VB} and the E_{CB} of HTNT, in reference to anatase. This could be the origin of the increase of the V_{oc}, since E_{redox} and the ratio n_c/N_{CB}(where n_c and N_{CB} corresponds to the electrons in the conduction band and the total number of electronic states in the CB) it is expected to be similar for both materials (see Eq. (1)) [42]. The reduction of the Φ_{HTNT} can be understood in terms of the H-atom passivation of the surface, what is particularly interesting for that polymorph, since it can keep a good band gap with a comparative lower work function.

$$V_{OC} = \frac{1}{q_e}\left(E_{CB} + k_B T \ln\left(\frac{n_c}{N_{CB}}\right) - E_{redox}\right) \quad (1)$$

$$J_{SC} = \int_{\lambda} LHE(\lambda)\Phi_{inject}\eta_{collect}\, d\lambda \quad (2)$$

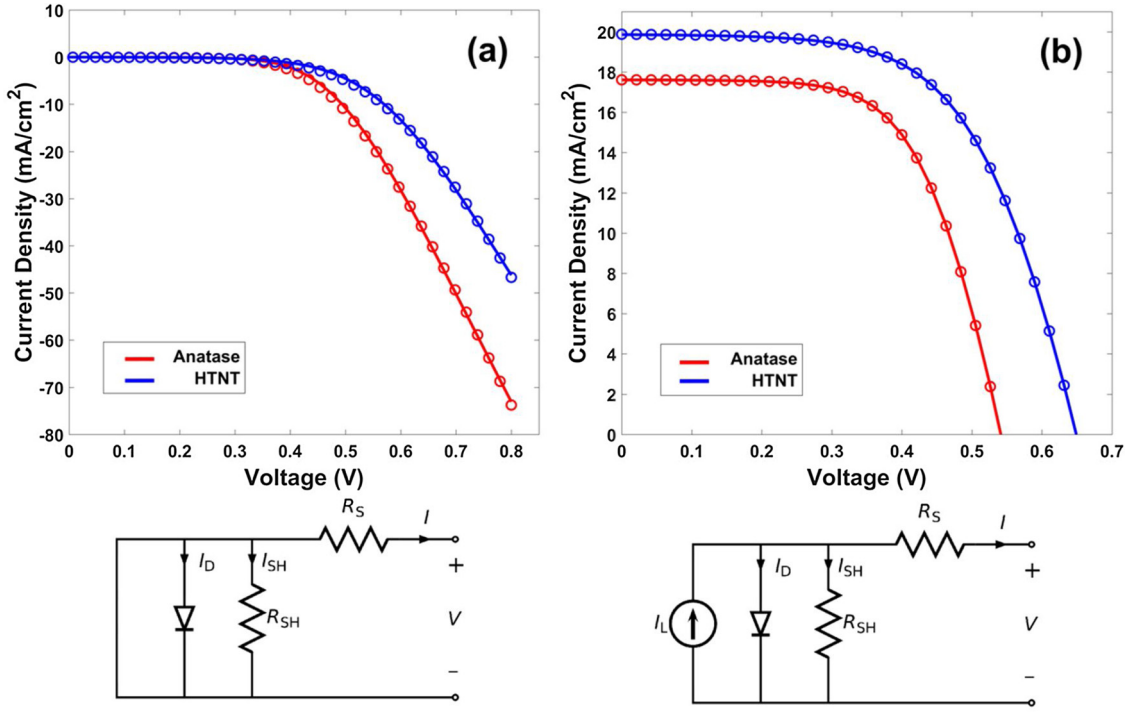

Fig. 5. Current Density – Voltage (J–V) curve for HTNT and anatasein dark conditions (a) and under AM1.5 illumination. Equivalent circuit models, utilized for the fitting procedure of J–V curves are presented.

Table 1
Photovoltaic parameters for the electrical characterization of the anatase- and HTNT-DSSCs according to the circuit presented in Fig. 4 (f).

	Anatase	HTNT
R_{SH}(kΩ)	2.73(10)	1.27(2)
R_S(Ω)	11.15(58)	13.49(12)
J_{sc}(mA. cm^{-2})	17.59(13)	19.79(8)
J_{max}(mA. cm^{-2})	15.36(6)	16.76(8)
V_{oc}(V)	0.538(5)	0.643(12)
V_{max}(V)	0.391(3)	0.448(10)
FF	0.64(1)	0.59(1)
η(%)	**5.95(10)**	**7.63(8)**

Table 2
Resistance (R_D) and time constants (τ_D/τ_L) parameters for Anatase and HTNT cells under dark and AM 1.5 illumination conditions.

	Anatase				HTNT			
	R_D(kΩ)	τ_D	τ_L	τ_D/τ_L	R_D(kΩ)	τ_D	τ_L	τ_D/τ_L
400 mV	23.9	0.0054	0.0051	1.059	18.2	0.0041	0.0036	1.139
450 mV	29.3	0.0057	0.0047	1.213	21.7	0.0043	0.0027	1.593
500 mV	31.6	0.0058	0.0032	1.813	27.2	0.0047	0.0021	2.238
550 mV	35.9	0.0061	0.0027	2.259	32.4	0.0053	0.0017	3.118

One additionally interesting fact is that injection efficiency (Φ_{inject}) and the charge collection efficiency ($\eta_{collect}$) for N719 dye on HTNT is adequate, as reflected from the increase of the J_{sc} according to Eq. (2). Since the same dye is utilized, the light harvesting efficiency (LHE)can

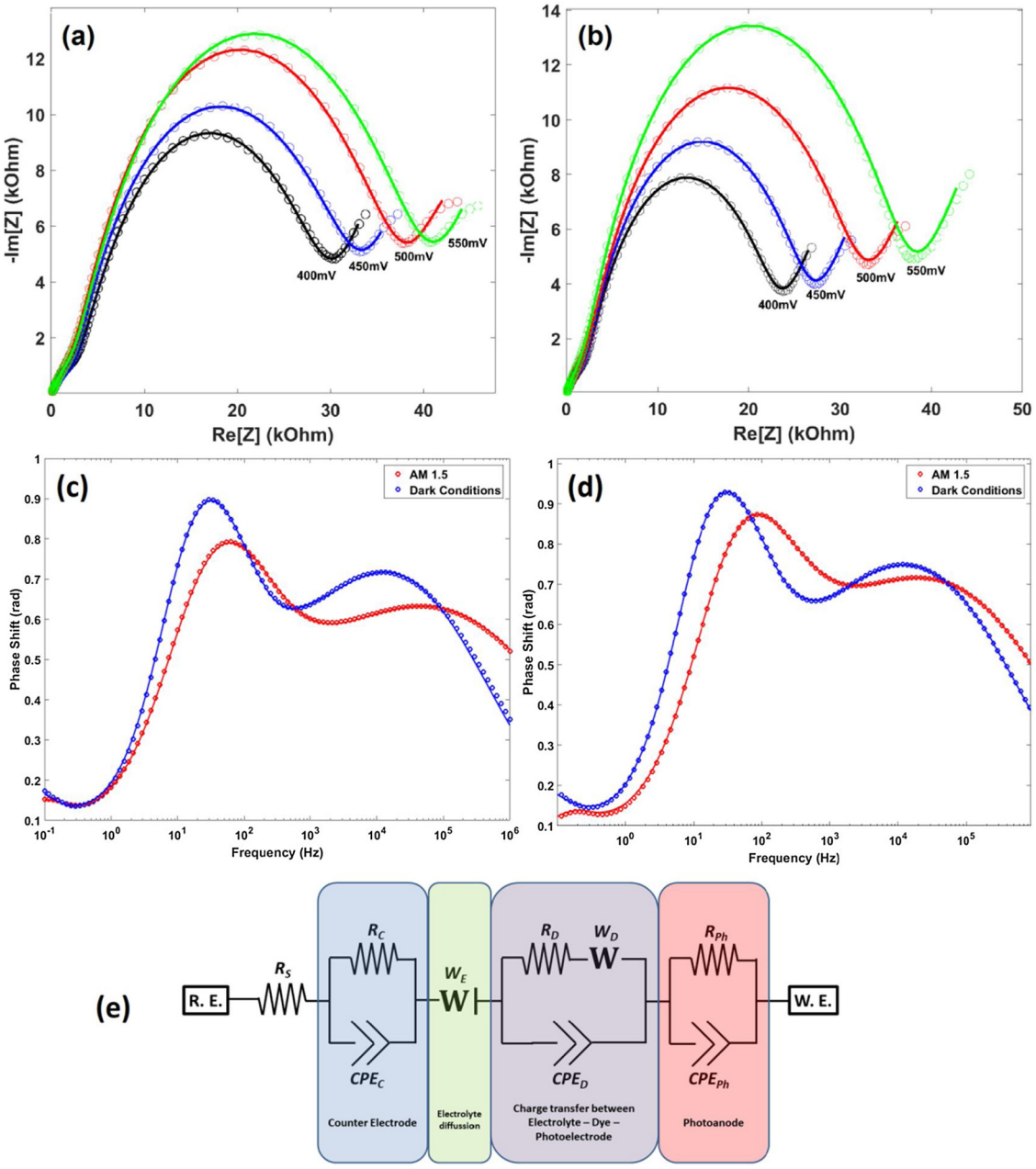

Fig. 6. Nyquist plots for (a) Anatase and (b) HTNTs DSSC measured under AM 1.5 illumination conditions at different applied bias. Phase shift plots for (c) Anatase and (d) HTNTs DSSC at 550 mV applied bias. (e) The circuit model used in the fitting of EIS data curves of both solar cells. Note: R.E. is the reference electrode and W.E. the working electrode.

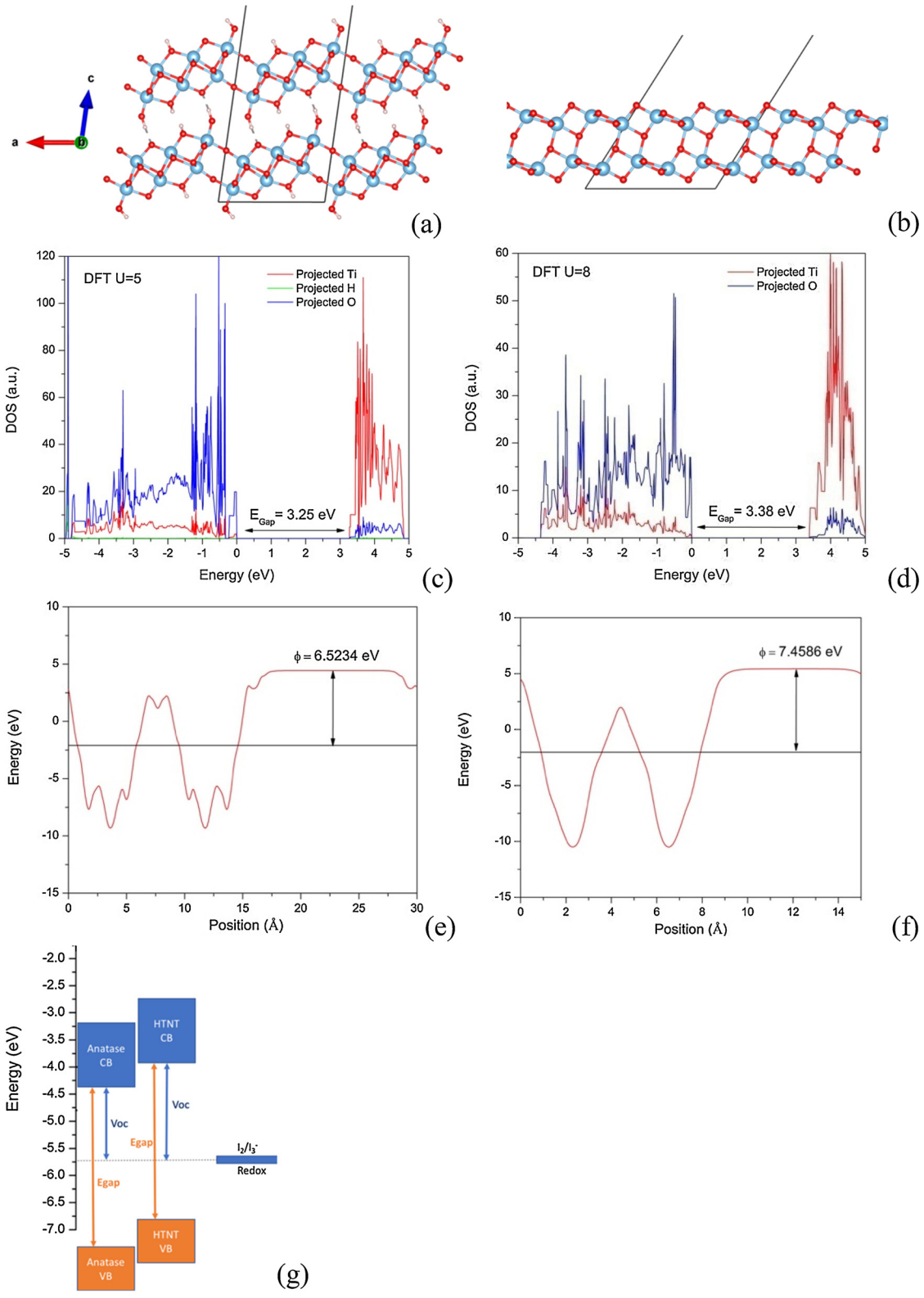

Fig. 7. Crystal structure of the 2D-Slab model for HTNT (a) and Anatase (b), the corresponding projected density of states (c) and (d); and the work function for both polymorphs (e) and (f). The band alignment scheme is presented in (g).

be considered as constant when comparing with both photoelectrodes. It is probably that the highly porous surface with an enhanced V_{oc}, is the key of utilizing HTNT as DSSC photoelectrode.

4. Conclusions

In this work, we presented the performance of HTNT for DSSC applications. We obtained an increase in efficiency of the solar cell, which is about ~28% higher when compared to anatase based DSSC. This

enhancement could be explained in terms of open-circuit voltage, directly associated to the value of the HTNT band gap (E_{gap} = 3.3 eV) and the relative position of the edge conduction band; and the increase of the short-circuit current, directly associated to the enhancement of the specific area of the photoelectrode. All these characteristics were obtained from the full experimental and theoretical characterization of the system. We expect that this system could be further characterized, utilizing different dyes or absorbers, in order to evaluate the potential use of hydrogen titanate nanotubes for solar cell applications.

5. Competing financial interests

The authors declare no competing financial interests.

Acknowledgments

The authors wish to thank the Uruguayan funding institutions CSIC, ANII and PEDECIBA, and the Brazilian ones CNPQ and FAPESC. We would like to thank the financial support provided by the EQC-X-2012-1-14 research project. We specially acknowledge to Álvaro Camargo at the “Servicio de Microscopia Electrónica de Barrido - Centro Universitario de Tacuarembó –UdelaR” for SEM images.

References

[1] B. O’Regan, M. Grätzel, Nature 353 (1991) 737–740.
[2] S. Mathew, A. Yella, P. Gao, R. Humphry-Baker, F.E. CurchodBasile, N. Ashari-Astani, I. Tavernelli, U. Rothlisberger, K. NazeeruddinMd, M. Grätzel, Nat. Chem. 6 (2014) 242–247.
[3] R. Faccio, L. Fernández-Werner, H. Pardo, A.W. Mombrú, Recent Pat. Nanotechnol. 5 (2011) 46–61.
[4] C.C. Raj, R. Prasanth, J. Power Sources 317 (2016) 120–132.
[5] V. Sugathan, E. John, K. Sudhakar, Renew. Sustain. Energy Rev. 52 (2015) 54–64.
[6] E.M. Waleed, J. Phys. D: Appl. Phys. 42 (2009) 155502.
[7] R. Jose, V. Thavasi, S. Ramakrishna, J. Am. Ceram. Soc. 92 (2009) 289–301.
[8] P. Roy, D. Kim, K. Lee, E. Spiecker, P. Schmuki, Nanoscale 2 (2010) 45–59.
[9] J.R. Jennings, A. Ghicov, L.M. Peter, P. Schmuki, A.B. Walker, J. Am. Chem. Soc. 130 (2008) 13364–13372.
[10] D. Kim, A. Ghicov, S.P. Albu, P. Schmuki, J. Am. Chem. Soc. 130 (2008) 16454–16455.
[11] D. Kim, A. Ghicov, P. Schmuki, Electrochem. Commun. 10 (2008) 1835–1838.
[12] A. Ghicov, S.P. Albu, R. Hahn, D. Kim, T. Stergiopoulos, J. Kunze, C.-A. Schiller, P. Falaras, P. Schmuki, Chemistry – An. Asian J. 4 (2009) 520–525.
[13] K. Zhu, N.R. Neale, A. Miedaner, A.J. Frank, Nano Lett. 7 (2007) 69–74.
[14] D. Kuang, J. Brillet, P. Chen, M. Takata, S. Uchida, H. Miura, K. Sumioka, S.M. Zakeeruddin, M. Grätzel, ACS Nano 2 (2008) 1113–1116.
[15] T. Stergiopoulos, A. Ghicov, V. Likodimos, D.S. Tsoukleris, J. Kunze, P. Schmuki, P. Falaras, Int. J. Biomed. Nanosci. 19 (2008) 235602.
[16] L. Kavan, B. O’Regan, A. Kay, M. Grätzel, J. Electroanal. Chem. 346 (1993) 291–307.
[17] M.K. Nazeeruddin, A. Kay, I. Rodicio, R. Humphry-Baker, E. Mueller, P. Liska, N. Vlachopoulos, M. Graetzel, J. Am. Chem. Soc. 115 (1993) 6382–6390.
[18] N.G. Park, G. Schlichthörl, J. van de Lagemaat, H.M. Cheong, A. Mascarenhas, A.J. Frank, J. Phys. Chem. B 103 (1999) 3308–3314.
[19] S. Ito, P. Liska, P. Comte, R. Charvet, P. Pechy, U. Bach, L. Schmidt-Mende, S.M. Zakeeruddin, A. Kay, M.K. Nazeeruddin, M. Gratzel, Chem. Commun. (2005) 4351–4353.
[20] B.C. O’Regan, J.R. Durrant, P.M. Sommeling, N.J. Bakker, J. Phys. Chem. C 111 (2007) 14001–14010.
[21] P. Roy, D. Kim, I. Paramasivam, P. Schmuki, Electrochem. Commun. 11 (2009) 1001–1004.
[22] C.-J. Lin, W.-Y. Yu, S.-H. Chien, J. Mater. Chem. 20 (2010) 1073–1077.
[23] L. Fernández-Werner, F. Pignanelli, B. Montenegro, M. Romero, H. Pardo, R. Faccio, Á.W. Mombrú, J. Energy Storage 12 (2017) 66–77.
[24] A. Berni, M. Mennig, H. Schmidt, Doctor Blade, M.A. Aegerter, M. Mennig (Eds.), Sol-Gel Technologies for Glass Producers and Users, Springer US, Boston, MA, 2004, pp. 89–92.
[25] P. Hohenberg, W. Kohn, Phys. Rev. 136 (1964) B864–B871.
[26] W. Kohn, L.J. Sham, Phys. Rev. 140 (1965) A1133–A1138.
[27] G. Kresse, J. Furthmüller, Phys. Rev. B 54 (1996) 11169–11186.
[28] G. Kresse, J. Furthmüller, Comp. Mater. Sci. 6 (1996) 15–50.
[29] G. Kresse, J. Hafner, Phys. Rev. B 47 (1993) 558–561.
[30] G. Kresse, J. Hafner, Phys. Rev. B 49 (1994) 14251–14269.
[31] G. Kresse, D. Joubert, Phys. Rev. B 59 (1999) 1758.
[32] P.E. Blöchl, Phys. Rev. B 50 (1994) 17953–17979.
[33] G. Kresse, D. Joubert, Phys. Rev. B 59 (1999) 1758–1775.
[34] J.P. Perdew, K. Burke, M. Ernzerhof, Phys. Rev. Lett. 77 (1996) 3865–3868.
[35] J.P. Perdew, K. Burke, M. Ernzerhof, Phys. Rev. Lett. 78 (1997) 1396-1396.
[36] S.L. Dudarev, G.A. Botton, S.Y. Savrasov, C.J. Humphreys, A.P. Sutton, Phys. Rev. B 57 (1998) 1505–1509.
[37] E. German, R. Faccio, A.W. Mombrú, Appl. Surf. Sci. (2017).
[38] E. German, R. Faccio, Á.W. Mombrú, Appl. Surf.. Sci. 426 (2017) 1182–1189.
[39] M. Adachi, M. Sakamoto, J. Jiu, Y. Ogata, S. Isoda, J. Phys. Chem. B 110 (2006) 13872–13880.
[40] C.-P. Hsu, K.-M. Lee, J.T.-W. Huang, C.-Y. Lin, C.-H. Lee, L.-P. Wang, S.-Y. Tsai, K.-C. Ho, Electrochim. Acta 53 (2008) 7514–7522.
[41] Q. Wang, J.-E. Moser, M. Grätzel, J. Phys. Chem. B 109 (2005) 14945–14953.
[42] S. Bagheri Novir, S.M. Hashemianzadeh, Spectrochim. Acta, Part A 143 (2015) 20–34.